Journal of Environmental Chemical Engineering 11 (2023) 111478

Contents lists available at ScienceDirect

Journal of Environmental Chemical Engineering

journal homepage: www.elsevier.com/locate/jece

How bimetallic CoMo carbides and nitrides improve CO oxidation

Yanet Villasana [a,*], Jorge A. García-Macedo [b], Andrea Navarro-Puyuelo [c], Mourad Boujnah [d], Inés Reyero [c], Hugo A. Lara-García [e], Jesús Muñiz [f], Fernando Bimbela [c], Luis M. Gandía [c], Joaquin L. Brito [a,g], Franklin J. Méndez [h,*]

[a] Biomass Laboratory, Biomass to Resources Group, Universidad Regional Amazónica IKIAM, Tena, Ecuador
[b] Departamento de Estado Sólido, Instituto de Física, Universidad Nacional Autónoma de México, Ciudad Universitaria, Ciudad de México 04510, Mexico
[c] Grupo de Reactores Químicos y Procesos para la Valorización de Recursos Renovables, Institute for Advanced Materials and Mathematics (InaMat2), Universidad Pública de Navarra (UPNA), Pamplona, Spain
[d] Laboratorio Nacional de Proyección Térmica (CENAPROT), Centro de Investigación y de Estudios Avanzados (CINVESTAV-IPN), Fracc. Real de Juriquilla, Querétaro 76230, Mexico
[e] Departamento de Física Química, Instituto de Física, Universidad Nacional Autónoma de México, Ciudad Universitaria, Ciudad de México 04510, Mexico
[f] Instituto de Energías Renovables, Universidad Nacional Autónoma de México, Priv. Xochicalco s/n, Temixco 62580, Morelos, Mexico
[g] Centro de Química Dr. Gabriel Chuchani, Instituto Venezolano de Investigaciones Científicas, Carretera Panamericana Km 11 Altos de Pipe, Caracas 1020A Venezuela
[h] Centro de Investigación en Ciencia Aplicada y Tecnología Avanzada, CICATA Morelos, Instituto Politécnico Nacional, Boulevard de la Tecnología 1036 Z-1, P 2/2, Atlacholoaya 62790, Xochitepec, Mexico

ARTICLE INFO

Editor: Carlos Grande

Keywords:
Carbides
CO oxidation
CoMo-based catalysts
Nitrides

ABSTRACT

CO elimination is an important step for the proper management of gaseous effluents from various processes, thus avoiding adverse impacts on the environment and human health. In this study, different bimetallic Al_2O_3-supported CoMo catalysts have been developed, characterized, and tested in the CO oxidation reaction, based on their respective oxides, carbides, and nitrides phases. The parent CoMo-oxide catalyst (CoMo) was prepared by impregnation and then transformed to its carburized (CoMoC) and nitrided (CoMoN) forms using temperature-programmed reaction methods under controlled atmospheres of CH_4/H_2 and NH_3, respectively. The catalytic results demonstrate that the CoMoC catalyst exhibits higher activity compared to its CoMoN counterpart, and both are more active than the parent CoMo catalyst. Furthermore, the reduction temperature and space velocity were key process factors, which notably influenced activity and kinetic parameters, while the increase of reduction time does not seem to improve catalytic behavior. These results were associated with a better metal dispersion, and relatively higher reduction grade and metallic surface area on the carbides and nitrides, opening the possibility that new adsorption sites may be created. The catalytic results compare favorably with other non-noble metal catalysts, such as Cr-, Cu-, Fe-, and Ni-based samples, and highlight the potential of using carbides and nitrides as alternative formulations to enhance the performance of CO oxidation.

1. Introduction

The World Health Organization (WHO) states that air pollution threatens public health and the climate of our planet. They report that the chemicals with the strongest evidence of adverse effects on public health include particulate matter (PM), carbon monoxide (CO), ozone (O_3), nitrogen dioxide (NO_2), and sulfur dioxide (SO_2) [1]. For this reason, regulations regarding emissions from vehicles and industries have been proposed worldwide [2].

Carbon monoxide is a flammable and toxic gas that is often generated by incomplete combustion of fuels in vehicles, power generation plants, chemical industries, refinery processes, and certain bioenergy generation technologies [3]. Despite its fundamental importance as one of the main constituents of syngas, which is a key intermediate in the chemicals and synthetic fuels industries [4], CO, when present in low concentrations in exhaust gases from industrial and power generation processes, becomes a co-pollutant that poses significant hazards and threats. Therefore, CO contributes to air pollution and has negative effects on human health and ecosystems [1–3,5]. This pollutant can be removed through methods such as adsorption [6], methanation [7], or

* Corresponding authors.
E-mail addresses: yanet.villasana@ikiam.edu.ec, ytvillas@gmail.com (Y. Villasana), fmendez@ipn.mx, frankmendez.mz@gmail.com (F.J. Méndez).

https://doi.org/10.1016/j.jece.2023.111478
Received 8 August 2023; Received in revised form 28 October 2023; Accepted 11 November 2023
Available online 20 November 2023

catalytic oxidation [8], the latter being one of the most effective purification technologies. For instance, catalytic preferential oxidation (PROX) of CO is a key technology used to purify H_2-rich streams and prevent the poisoning of Pt anodes in polymer-electrolyte membrane fuel cells (PEMFCs) [9]. Another important catalytic technology that targets CO oxidation is the Selective Catalytic Reduction (SCR) of industrial flue gases, e.g., in desulfurization processes [10]. It is an efficient method for purifying these flue gas streams, but it is highly dependent on relevant process conditions, namely gas composition and reaction conditions, among others. In this regard, CO catalytic oxidation in flue gases presents two major problems: poisoning of the catalyst's active centers and uncontrollable emissions at medium and low operating temperatures [11]. The former can be derived from the presence of S- and P-containing compounds in the exhaust gases, which are originated from certain fuels and lubricants [12], whereas the latter is a consequence of the unavoidable cold-start regime that takes place in the first minutes of operation of an internal combustion vehicle. This regime makes it impossible for the catalytic converter to effectively perform below 200 °C [13].

In the last 40 years, catalytic oxidation of CO has been developed mostly using noble metal-based catalysts (Au, Pt, Pd, Rh), not only because of their high activity but also due to their excellent potential to study the structure-reactivity relationship [14–17]. However, despite their good performance, its further application has been limited due to difficulties in reusability, high-temperature sintering, high costs, and low abundance on Earth. Therefore, recent studies have focused on designing newer, more economical catalytic systems that could increase CO conversion without serious poisoning problems, especially during the cold start of internal combustion engines [3,18–22]. This is the moment when untreated CO is emitted into the atmosphere, thus raising pollution levels [5,23].

Several alternatives with non-noble catalysts have been proposed for CO oxidation so far, which have been discussed in comprehensive reviews [8,19,23,24]. Ceria catalysts have been studied in depth and modified by different active metals, resulting in a decrease in the energy formation of the oxygen vacancy, improving spillover effects and surface area, while increasing catalytic activity [5,25]. Zhang et al. recently proposed oxygen-functionalized MBenes with orthorhombic and hexagonal crystal structures, denoted as orth-$M_2B_2O_2$ and hex-M_2B_2O (M = Ti, V, Cr, Zr, Nb, Mo, Hf, Ta, and W) [26]. The hexagonal Mo, V, and Cr-based materials exceeded the catalytic activity of CeO_2, while orthorhombic analogous showed even higher catalytic activity than Pt-CeO_2 and Au-CeO_2. Another recent study has proposed binary (MnCe, MnZr) and ternary (MnZrCe) oxides as catalysts for CO oxidation [27]. Furthermore, some experimental and theoretical studies have reported promising results using catalysts based on early transition metal oxides, including Cu_2O [28], CuO/Al_2O_3 [29], Co oxides used either standalone (unsupported) or as supports for Pt catalysts [30], and NiO/Al_2O_3 [31], among others.

The use of metal-carbide surfaces as support of efficient catalysts for CO oxidation, desulfurization, and hydrogenation reactions has been proposed too. Metals such as Au, Cu, Ni, and Pt form two or three-dimensional islands depending on the level of coverage when growing on the carbide substrates [32]. These structures promote the ability to dissociate O_2 and perform the $2CO + O_2 \rightarrow 2CO_2$ reaction, which is attributed to the preferential formation of noble metal-C bonds with significant electronic perturbations in the noble metal. To the best of our knowledge and understanding, there has been a significant absence of studies on using supported carburized or nitrided metal phases in CO catalytic oxidation. These types of phases exhibit extraordinary hardness, high electrical and thermal conductivity, good corrosion resistance, high wear resistance, both chemical and physical, and low coefficient of friction, which makes these materials very attractive from the point of view of their commercial applications [24,33].

For all these reasons, the general objective of the present study is to provide insight into the use of early transition metal carbides or nitrides as efficient catalysts for CO oxidation, which could constitute a lower-cost alternative to noble metal-based catalysts. We propose the utilization of conventional Al_2O_3-supported CoMo catalysts and their chemical transformation into their analogous bimetallic carbides and nitrides phases. To achieve this objective, we investigated the effects of catalytic phases, reduction parameters, and reaction conditions on their performance in CO oxidation through their kinetic behavior.

2. Methodology

2.1. Catalysts preparation

The catalysts were prepared using a well-known procedure as incipient wetness impregnation of metal salts and calcination to obtain oxidic precursors, followed by a temperature-programmed reaction method according to our previously reported articles [34–36]. Ammonium heptamolybdate tetrahydrate ($(NH_4)_6Mo_7O_{24}{\cdot}4H_2O$, 81–83 % MoO_3 basis, Sigma-Aldrich) and cobalt(II) nitrate hexahydrate ($Co(NO_3)_2{\cdot}6H_2O$, ACS reagent, ≥ 98 %, Sigma-Aldrich) were used as Mo and Co oxides precursors, while a commercial Al_2O_3 (Alfa Aesar, metal basis, 99 %) was used as support. After impregnation, catalysts were calcined at 500 °C for 4 h to obtain the oxide catalyst, and then two portions were subjected to a temperature-programmed reaction using a tubular quartz reactor and heating up to 700 °C for 2 h in the presence of a gas flow composed of a mixture of CH_4/H_2 (20 vol% of CH_4 in H_2, 100 mL/min) or NH_3 (100 %, 100 mL/min) for carbide or nitride catalysts, respectively. These two last catalysts were passivated using a flow rate of 50 mL/min of diluted oxygen (1 vol% O_2 in Ar) for 45 min to avoid spontaneous pyrophoric reactions. The Co/Co + Mo) atomic ratio of all catalysts was approximately 0.33, and the total loading of metal oxide was set at 15 wt%. The obtained catalytic materials were denoted as CoMo, CoMoN, and CoMoC for the oxide, nitride, and carbide, respectively.

2.2. Physicochemical characterization

2.2.1. Morphological and elemental analysis

The scanning electron microscopy (SEM) images and apparent (semiquantitative) composition of the catalysts by energy-dispersive X-ray spectroscopy (EDS) were acquired using an Oxford microanalyzer model 7582 coupled to a JEOL JSM-6390 microscope. The mapping process usually lasted around 30 min, and the analysis covered a range of a few micrometers in scale.

2.2.2. Inductively coupled plasma-optical emission spectroscopy

To determine the actual Co and Mo metallic contents in the catalysts, elemental analysis by ICP-OES analysis was also performed. The analyses were conducted by the *Servicio de Análisis Químico* of the *Servicio de Apoyo a la Investigación (SAI)* of the University of Zaragoza (Spain), using a Thermo Elemental IRIS INTREPID RADIAL spectrophotometer.

2.2.3. Nitrogen physisorption

The textural properties were determined using nitrogen physisorption data obtained with an Anton Paar NOVAtouch® LX2 automatic analyzer. Prior to analysis, the samples were degassed at 90 °C for 2 h, followed by 10 h at 220 °C. The specific surface area (S_{BET}) was calculated using the Brunauer-Emmett-Teller method, the pore volume (V_p) was measured at $P/P_0 = 0.98$, and the average pore diameter (D_p) was determined from the maximum value of the pore size distribution, calculated using the Barrett-Joyner-Halenda method from the desorption branch.

2.2.4. X-ray diffraction

The diffractograms were obtained using a Bruker D8 Advance diffractometer equipped with a CuKα radiation source at 1.5456 Å. Phase identification was conducted using the International Centre for

Diffraction Data (ICDD) through X'Pert HighScore Plus software with the PDF-2 database [37].

2.2.5. High-resolution transmission electron microscopy

HRTEM images were obtained with a Jeol 2010 microscope operating with a LaB_6 cathode at 200 kV. The bimetallic oxide and nitride catalysts were placed on a 300-mesh Cu grid coated with collodion, while carbide analogs were placed on an Au grid. In all cases, the samples were plasma-treated for 2 mins before being introduced into the microscope. The DigitalMicrograph software v.2.32.888.0, also known as the Gatan Microscopy Suite, was used to perform the analysis of the images obtained here [38], while the visualization of indexed structures and their respective crystallographic planes was achieved using the VESTA program [39].

2.2.6. Raman spectroscopy

A Horiba XploRA™ plus spectrometer, equipped with a 50x objective lens and a laser beam excitation at $\lambda = 532$ nm, was used to obtain Raman spectra for both the support and catalysts. The samples were prepared in pellet form to prevent any movement within the sample holder, and the laser power was adjusted to avoid uncontrolled thermal effects. The acquisition time was set at 12 s and typically averaged over 10 accumulations to improve the signal-to-noise ratio.

2.2.7. Ultraviolet-visible diffuse reflectance spectroscopy

The optical spectra were obtained with the UV–vis DRS technique using a Perkin Elmer Lambda-900 UV/VIS/NIR spectrophotometer with a LabSphere® PELA-1020 diffusion reflection attachment.

2.2.8. Hydrogen temperature-programmed reduction

The reducibility data were collected using a Micromeritics AutoChem II 2920 automatic analyzer equipped with a thermal conductivity detector (TCD). The catalysts were reduced using 75 N mL/min of H_2 diluted in Ar (5 vol% H_2) from room temperature to 950 °C under a 5 °C/min temperature ramp.

2.2.9. CO pulse chemisorption on reduced catalysts

CO pulse chemisorption analyses were conducted in a Micromeritics AutoChem II 2920 apparatus equipped with a TCD. The catalysts were pre-reduced at 400 °C for 1 h using a heating rate of 10 °C/min under a 50 N mL/min H_2 flow. Then, the samples were cooled under He flow until reaching the analysis temperature, around 30 °C. Finally, dynamic pulse chemisorption was conducted using a mixture of 10 vol% CO in He.

2.2.10. Diffuse reflectance infrared Fourier transform spectroscopy of adsorbed CO and NO molecules on reduced catalysts

The CO and NO interactions with the surface of the reduced catalysts were studied using a Thermo Scientific Nicolet iS50 spectrophotometer equipped with a PIKE DifussIR DRIFTS cell. The samples were directly placed in the reaction chamber and reduced *in situ* at 400 °C for 1 h using 30 mL of H_2/N_2 mixture (10 vol% of H_2). After reduction, the catalysts were purged with He (30 mL/min) for 30 min, cooled to 20 °C, and saturated with a CO/He mixture (5 vol% of CO, 30 mL/min flow) or NO/He mixture (2 vol% of NO, 30 mL/min flow). All spectra were collected using 128 scans with a resolution of 4 cm^{-1}, employing an MCT detector.

2.3. Catalytic performance

2.3.1. Catalyst activation

At least one day before performing the activity tests, the catalysts were reduced *in situ* by flowing pure hydrogen at a rate of 30 mL/min, at a temperature of 300, 400, or 500 °C, during 1 or 4 h, using a vertical fixed-bed reactor (Pyrex® tube, 400 mm long, and 15 mm i.d.).

2.3.2. Temperature-programmed CO oxidation tests

The reactions were carried out under atmospheric pressure, using a catalyst volume of 0.5 cm^3 that corresponded to *ca.* 50 mg of sample. The gas-feeding mixture (1 vol% CO and 1 vol% O_2 diluted in N_2) was introduced in the reactor in a downflow configuration at a flow rate of 30 or 50 mL/min; these flow rate values correspond to a molar flow rate of CO at about 2.23×10^{-7} mol/s (gas hourly space velocity, GHSV = 3600 h^{-1}) or 3.72×10^{-7} mol/s (GHSV = 6000 h^{-1}), respectively.

CO and CO_2 compositions were determined while ramping up the temperature to 350 °C, with samples taken at 10 °C intervals (± 3 °C). An online Perkin Elmer Clarus® 500 gas chromatograph, equipped with a flame ionization detector (FID) and TotalCrom Workstation software, was used to obtain and process the data. CO conversion (X_{CO}) and specific reaction rate (r) were calculated according to Eqs. (1) and (2), respectively.

$$X_{CO} = \left(\frac{[CO]_{inlet} - [CO]_{outlet}}{[CO]_{inlet}}\right) \quad (1)$$

$$r = \left(\frac{X_{CO} \times F_{CO}}{m_{cat}}\right) \quad (2)$$

The activation energy (E_a) was determined under a kinetic control regime, with CO conversions below 20 %, by applying the linear Arrhenius Law (Eqs. 3 and 4). In these equations, $[CO]_\alpha$ represents the inlet or outlet CO concentrations, F_{CO} corresponds to the molar flow rate of CO, m_{cat} is the mass of the catalyst, A is the dimensionless pre-exponential factor, and R is the universal gas constant.

$$r = Ae^{\left(-\frac{E_a}{RT}\right)} \quad (3)$$

$$\ln(r) = -\frac{E_a}{R}\left(\frac{1}{T}\right) + \ln(A) \quad (4)$$

2.3.3. Stability tests

The CO oxidation reactions used in the stability tests were carried out following the procedure described in the previous section. In all experiments, the catalysts (~50 mg) were reduced at 400 °C in H_2 for 1 h, and during the reactions, the gas hourly space velocity was maintained at a constant value of 3600 h^{-1}, while the reaction temperatures were adjusted to achieve the desired conversion with the tested catalysts. Two different sets of reaction conditions were employed. First, the reactions were conducted under isothermal conditions (T = 250 °C), and then under isoconversion conditions (X_{CO} = 100 %). Reaction progress was monitored every 30 min continuously for 6 h, and the conversion was calculated using Eq. (1).

2.4. Density functional theory (DFT) calculations

DFT calculations were performed using the Vienna Ab initio Simulation Package (VASP) [40–42], and the projected augmented wave (PAW) method was adopted for the ion-electron interactions. The valence electrons for all systems were described by the generalized gradient approximation (GGA), in the form of the Perdew-Burke-Ernzerhof (PBE) functional [43]. A plane wave cutoff energy at 450 eV was selected. Geometry optimizations were carried out until the total energy and the maximum force were less than 10^{-5} eV/atom and 0.03 eV/Å, respectively. Vacuum space between two adjacent sheets was set at 20 Å or more, to eliminate the interaction between each other.

In order to evaluate the effect of van der Waals (vdW) interactions for the adsorption of CO molecule on the surface, the dispersion correction PBE+D3 was considered [44]. A gamma-centered (2 ×2 ×1) and (1 ×2 ×1) *k*-point grid was used to (220) and (511) surfaces Brillouin zone, respectively. The adsorption energies were calculated using Eq. (5).

$$E_{ads} = E_{adsorbed} - (E_{surface} + E_{CO}) \quad (5)$$

where $E_{adsorbed}$ refers to the energy of the system with the CO molecule adsorbed on the surface, and $E_{surface}$ is the energy of the clean surface. The value E_{CO} was obtained by placing an isolated CO molecule at the center of a 2.0 × 2.0 × 2.0 nm^3 unit cell; the Brillouin zone was sampled at the Γ-point only.

3. Results and Discussion

3.1. Physicochemical characterization of as-prepared catalysts

3.1.1. Morphology and elemental composition

SEM images and EDS spectra of CoMo, CoMoN, and CoMoC catalysts are shown in Fig. 1. The micrographs revealed some differences in their morphological characteristics. CoMo exhibited an irregular surface with no definite shape, whereas CoMoN and CoMoC appear more compact, indicating that the temperatures used for nitride and carbide preparation have promoted their packing. As expected, characteristic CoKα$_1$, MoLα$_1$, AlKα$_1$, and OKα$_1$ signals are detected in all EDS-analyzed samples, indicating the presence of such elements in the catalysts. NKα$_{1,2}$ and CKα$_{1,2}$ peaks are also observed in the CoMoN and CoMoC catalysts but were not quantified due to possible deviations by the adhesive used in the sample holder. It is worth noting that the EDS analysis also detected an extra signal attributed to CuLα in all the samples. The presence of this signal is unrelated to the catalyst composition but arises from the sample holder used during the analysis.

Table 1 shows the apparent and actual elemental composition of the catalysts obtained using SEM-EDS and ICP-OES, respectively. The results indicate that both the atomic composition and Co/(Co+Mo) ratios obtained by SEM-EDS were close to the nominal values (Table 1). Furthermore, the actual metallic contents obtained by ICP-OES were 1.1 wt% for Co and ranged between 5.8 and 5.9 wt% for Mo, which are also acceptable values for all the catalysts prepared in this work. As can be seen in the Electronic Supplementary Information (ESI, Fig. S1), the catalysts exhibit a homogeneous distribution of main elements throughout the entire sampled region, indicating the absence of selective element aggregation.

3.1.2. Textural characteristics

Fig. 2 presents the nitrogen physisorption isotherms and pore size distributions of the support as well as the CoMo, CoMoN, and CoMoC catalysts. The Al_2O_3 support exhibits a Type IV isotherm with a Type H2 hysteresis loop, which is a characteristic feature commonly found in mesoporous materials with spheroidal cavities, voids between spherical particles closely packed, or ink-bottle-shaped pores [45,46]. Furthermore, the type of isotherm remains unchanged after the metal impregnations in the CoMo catalyst and subsequent nitriding or carburizing processes in the CoMoN and CoMoC catalysts. However, the catalysts exhibit a narrower hysteresis loop as compared to the support. This reflects a slight decrease in the amount of adsorbed nitrogen, which

Table 1
Apparent and actual compositions of the catalysts obtained by SEM-EDS and ICP-OES.

Catalysts	Apparent composition by SEM-EDS			Actual composition by ICP-OES	
	Co (at%)	Mo (at%)	Co/ Co + Mo)	Co (wt%)	Mo (wt%)
CoMo	0.58	1.44	0.29	1.1	5.9
CoMoN	0.58	1.51	0.28	1.1	5.8
CoMoC	0.52	1.31	0.28	1.1	5.9

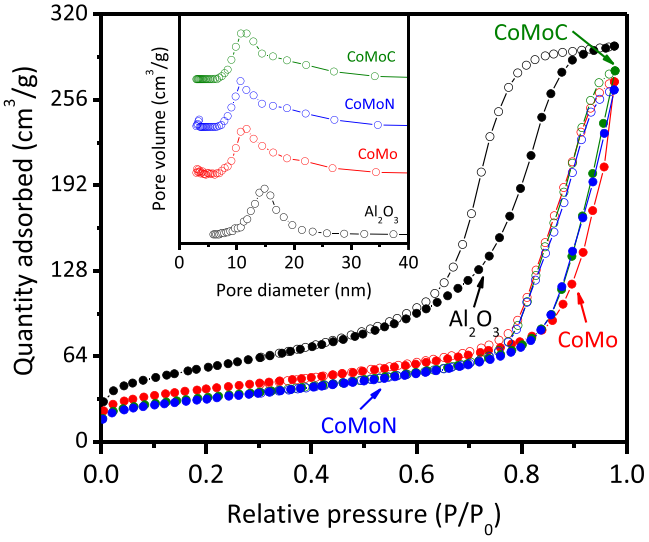

Fig. 2. Nitrogen physisorption isotherms and pore size distribution of the support and catalysts.

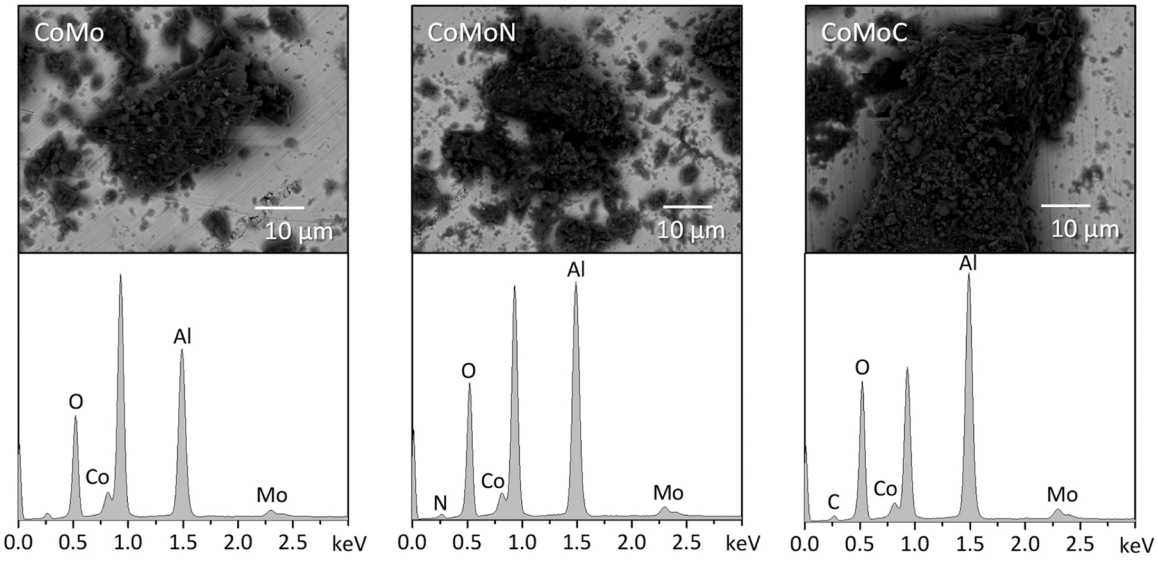

Fig. 1. SEM micrographs and EDS spectra of the catalysts.

consequently impacts the textural properties.

The textural properties of the support and catalysts were obtained from nitrogen physisorption data, and the results are summarized in Table 2. In this regard, the pore volume (V_p) remains relatively unchanged at approximately 0.4 cm^3/g, but the specific surface area (S_{BET}) decreased from 192 m^2/g in the Al_2O_3 support to 132, 118, and 112 m^2/g in the CoMo, CoMoN, and CoMoC catalysts, respectively. At the same time, a narrow pore size distribution ranging from 10 to 20 nm remains, but with different maxima. The pore diameter (D_p) of the support shows a larger size of approximately 14.9 nm, which decreases to 11.8 nm for the CoMo catalyst; this decrease in D_p is less significant for both the CoMoN and CoMoC catalysts (10.7 nm) when compared to the CoMo one. It is well known that the γ-Al_2O_3 structure remains essentially unchanged (no phase change, negligible porosity loss) during thermal treatments up to 750 °C [47]. Furthermore, C, N, and O are adjacent elements in the periodic table with similar atomic ratios, suggesting that their presence within the structure may not significantly alter the textural properties, which remain similar between the catalysts.

3.1.3. Structural properties

ESI files also show the XRD results obtained for both support and catalysts (Fig. S2). The diffractograms indicate the presence of γ-Al_2O_3 (PDF card number 00-029-0063) [37], with diffraction maxima observed at 2θ values of 37.64°, 45.83°, and 66.82°, corresponding to the (311), (400) and (440) crystallographic planes, respectively. Furthermore, the CoMo, CoMoN, and CoMoC catalysts only revealed signals from the support, likely due to the small particle size of the transition metal compounds, which are either below the detection limit of the technique, or highly dispersed in the support matrix. Therefore, HRTEM analysis was carried out on the as-prepared catalysts to provide detailed information about their atomic arrangement and crystal structure. The corresponding selected HRTEM images and the unit cell of indexed crystal structures with their observed crystallographic planes can be seen in Fig. 3a and b, respectively.

HRTEM images of the as-prepared CoMo catalyst reveal a spacing of approximately 3.3 Å characteristic of the (002) crystallographic plane. This plane corresponds to a monoclinic $CoMoO_4$ structure with space group C2/m (PDF card number 00-021-0868) [37]. On the other hand, when the oxidic catalyst was treated under ammonia flow to obtain the CoMoN catalyst, a lattice fringe of 2.1 Å corresponding to the (511) plane was clearly observed. This confirms the transformation from a monoclinic $CoMoO_4$ phase to a cubic Co_3Mo_3N structure with space group Fd-3 m (PDF card number 04-008-1301) [37]. In contrast, when the parent catalyst was thermally treated in a CH_4/H_2 atmosphere to obtain the CoMoC catalyst, nanoparticles with interplanar distances matching the Co_6Mo_6C phase were identified. The identification was accomplished by observing the (511) and (220) crystallographic planes, which exhibited interplanar distances of approximately 2.1 and 3.8 Å, respectively. The cubic arrangement of the bimetallic Co_6Mo_6C nanostructure was indexed with space group Fd-3 m (PDF card number 01-080-0338) [37].

The corresponding Fast Fourier Transform (FFT) images are shown in the inset of Fig. 3a. The spots were also indexed as diffraction planes corresponding to the (002) plane of monoclinic $CoMoO_4$, the (511) plane of cubic Co_3Mo_3N, and the (511) and (220) planes of cubic Co_6Mo_6C structures. These values agree with the unit cell and crystallographic planes shown in Fig. 3b. It is important to note that HRTEM and FFT analyses did not reveal any evidence of the formation of the spinel $CoAl_2O_4$ phase, observed later in the results of UV–vis DRS, or segregated monometallic phases in the catalysts, but the limited area analyzed by the technique does not definitively exclude the possibility of the formation of these nanostructures.

Table 2
Textural properties of the support and catalysts obtained through nitrogen physisorption.

Samples	S_{BET} (m^2/g)	V_p (cm^3/g)	D_p (nm)
Al_2O_3	192	0.46	14.9
CoMo	132	0.42	11.8
CoMoN	118	0.43	10.7
CoMoC	112	0.43	10.7

3.1.4. Vibrational properties

The Raman spectra of the support and the as-prepared catalysts are shown in Fig. 4. Firstly, it is evident that the support presents three weak vibration bands: the first signal at 380 cm^{-1} can be associated with Al-O stretching vibrations, while the signals at 501 and 622 cm^{-1} are attributed to Al-O-Al deformation, as previously identified in intermediate Al-hydroxides phases [48]. These bands are absent in the catalyst's spectra, indicating that localized analyses were performed on the dispersed nanocrystals, and the laser did not penetrate them to the support. Furthermore, as previously assigned by Mo et al. [49], the CoMo catalyst exhibits a signal at approximately 980 cm^{-1}, which corresponds to the symmetric vibrations of Mo═O bonds; this vibration band is typically observed in octahedrally coordinated polymeric molybdenum oxide species. The signal at 840 cm^{-1} is associated with the presence of the asymmetric stretching mode of the Mo-O-Mo bridge bond in octahedral molybdates (polymolybdate species), while the signal at 245 cm^{-1} is assigned to its deformation. Solís-Casados et al. confirmed these signals but also identified a possible Co-Mo interaction (signal at 920 cm^{-1}), formed as cobalt oxide interacts with polymerized molybdenum oxide and crystalline $CoMoO_4$ [50].

The CoMoN and CoMoC catalysts exhibit similar Raman spectra compared to the analog CoMo one, indicating the presence of an oxide layer on the surface covering the HRTEM-identified Co_3Mo_3N and Co_6Mo_6C phases (see Fig. 3). This aligns with the expected presence of a surface passivation layer used to stabilize the carbide and nitride catalysts during the synthesis (see Section 2.1), which are known to be sensitive to air. On the other hand, it is important to note that the main expected signals at 590 and 1100 cm^{-1} for Mo-N vibration [51] and 823 and 1000 cm^{-1} for Mo-C vibration [52] were not observed. Furthermore, the CoMoC catalyst did not show the characteristic D-band between 1250 and 1450 cm^{-1} or any signal related to the deposition of carbon species during its synthesis [53], which is consistent with both the presence of a passivation layer and the preparation of non-coked materials, respectively.

3.1.5. Electronic properties

The electronic properties of the Al_2O_3 support and Al_2O_3-supported CoMo catalysts in their oxide, carbide, and nitride states were determined in the 200–800 nm range using the UV–vis DRS technique; the corresponding spectra are shown in Fig. 5. The spectrum of the support exhibited a weak absorption signal in the UV region when compared to the catalysts. Transitions in the visible region were not observed due to the $2\,s^2 2p^6$ configuration of the Al^{3+} species, which prevents such transitions. The weak signal observed at about 299 nm could be attributed to the ligand-to-metal charge transfer (LMCT) from the O^{2-} ligand to the Al^{3+} species [54].

The spectra of the catalysts exhibited two significant differences compared to that of the support. First, the CoMo catalyst exhibited three distinct signals centered around 540, 577, and 632 nm. These signals are associated with d-d transitions of Co^{2+} ions in tetrahedral coordination to O^{2-} atoms, corresponding to the catalytically inactive $CoAl_2O_4$-associated triplet [55,56]. The preparation of CoMoN and CoMoC catalysts resulted in a decrease in the intensity of these signals, indicating an increase in the amount of catalytically active cobalt present in both catalysts. Furthermore, all catalysts presented a mixture of octahedral (O_h) and tetrahedral (T_d) coordination of Mo atoms, and their proportion depend on the catalyst's nature. As previously reported [57,58], the first characteristic band ranging from 232 to 233 nm is associated with Mo species in O_h and T_d symmetry, and the second signal at 260 nm

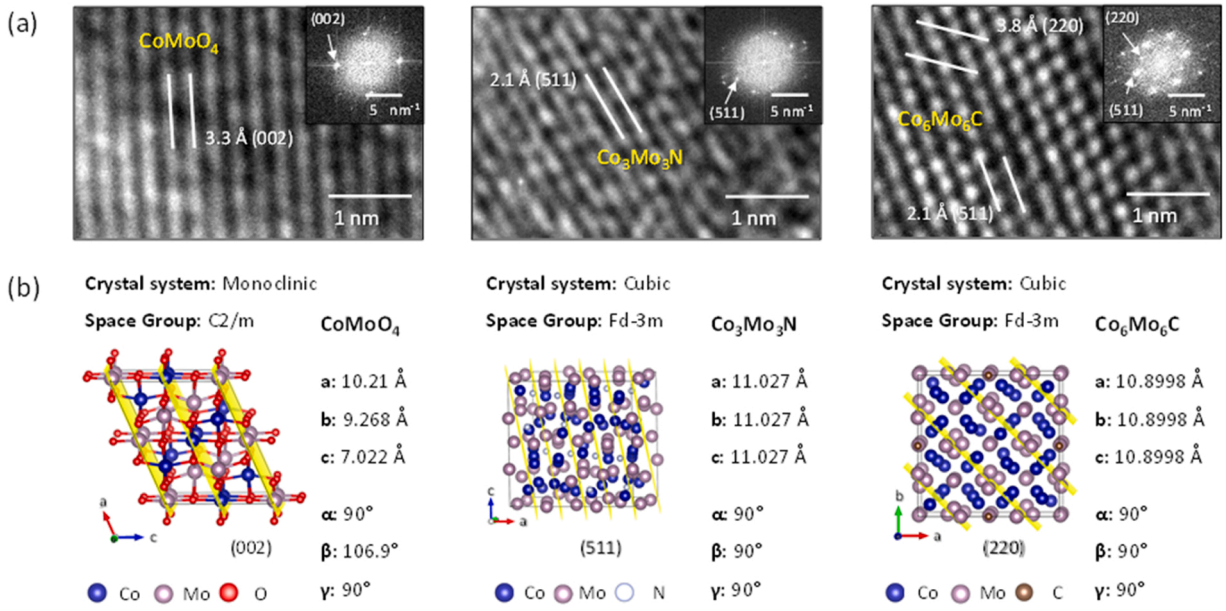

Fig. 3. (a) HRTEM images of the as-synthesized catalysts and the Fast Fourier Transform (FFT) obtained from the entire micrographs. (b) The unit cell of indexed $CoMoO_4$, Co_3Mo_3N, and Co_6Mo_6C crystal structures with their corresponding crystallographic planes obtained using the VESTA program [39].

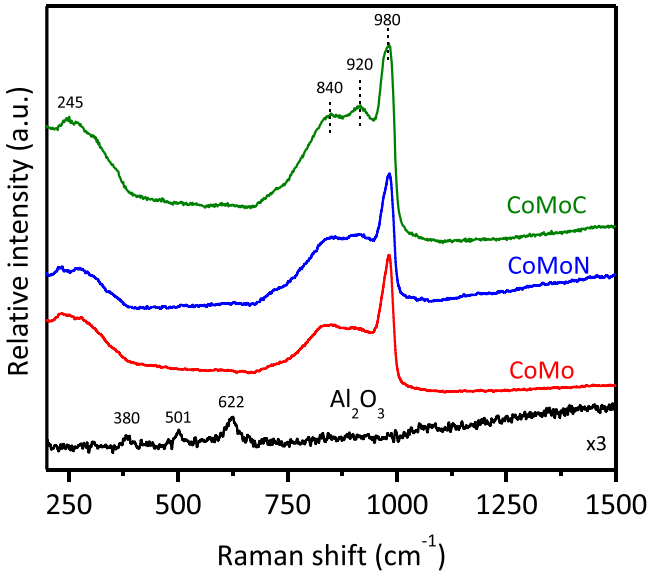

Fig. 4. Raman spectra of the support and catalysts.

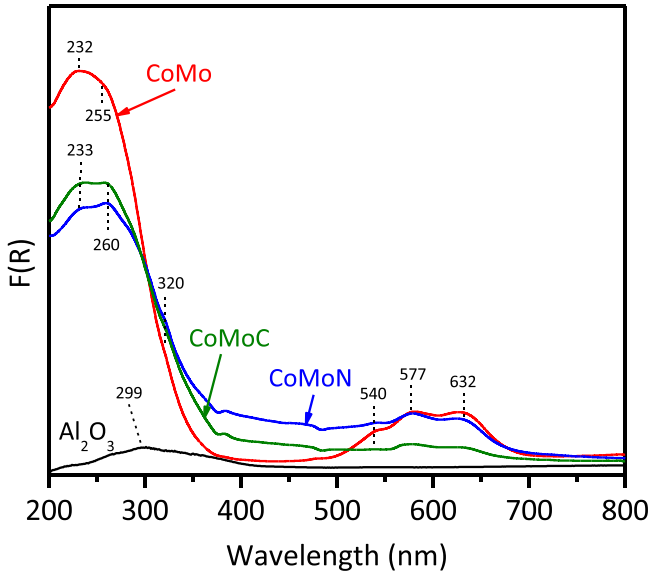

Fig. 5. UV–vis diffuse reflectance spectra of the support and catalysts.

corresponds to isolated species in T_d coordination; this last band is more resolved in CoMoC and CoMoN than in CoMo catalyst. CoMoN and CoMoC catalysts also showed an additional shoulder at approximately 320 nm that is associated with Mo in O_h coordination. These results give a hint that the CoMoN and CoMoC catalysts have a higher dispersion of Mo(O_h) species compared to the CoMo catalyst.

3.1.6. *Reducibility characteristics*

The H_2-TPR profiles for both the support and the Al_2O_3-supported CoMo catalysts are shown in Fig. 6. First, as expected, it can be seen that the support did not exhibit any significant reduction signal, which is consistent with the well-known irreducible nature of γ-Al_2O_3 below 950 °C [59]. Furthermore, the catalysts exhibit similar reduction profiles with two main signals. The first signal is characterized by a well-defined and intense reduction peak at a relatively low temperature with a maximum located between 430 and 450 °C, while the second one shows a broad and low-intensity signal at a higher temperature range between 770 and 781 °C. The low-temperature signal is usually associated with the first reduction step of well-dispersed octahedral Mo oxide species ($Mo^{6+} + 2e^- \rightarrow Mo^{4+}$) [60]. As that reduction peak also characterized the interaction between Mo-species and the Al_2O_3-support, a decrease in the reduction temperature maxima in this zone for the CoMoC (T_r = 436 °C) and CoMoN (T_r = 443 °C) catalysts indicates that the thermal treatment under controlled atmosphere promotes the decrease in the metal-support interaction (MSI) compared to the CoMo analogous (T_r = 453 °C). Furthermore, it is well known that the Co_3O_4 structure could be reduced to CoO, and then that CoO could be reduced to Co metallic in the same temperature range [61] but there is no evidence of such a phase on our catalysts. Similarly, $CoAl_2O_4$ should be reduced at higher temperatures, but reduction profiles did not reveal any significant hydrogen consumption peak, indicating that the process was hindered. This resistance could be attributed to the strong MSI,

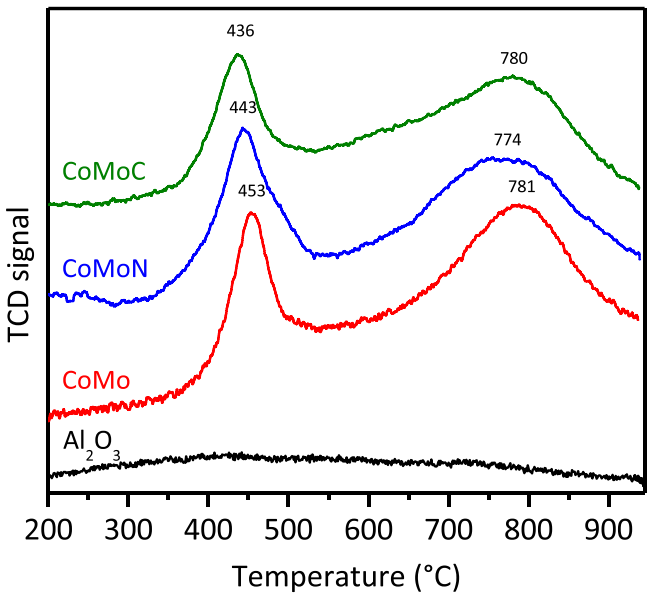

Fig. 6. H_2-TPR profiles of the support and catalysts.

making its reduction more difficult. The second signal at higher temperatures is assigned to the reduction of the isolated tetrahedral Mo species, plus the second reduction step of polymeric octahedral species ($Mo^{4+} + 2e^- \rightarrow Mo^0$) [60], which suggests the presence of different Mo species agglomerated coexisting in the same catalysts, as seen in the UV–vis DRS and Raman analysis.

Table 3 presents the quantitative data on hydrogen consumption and the degree of reduction for each catalyst. The results indicate that both the CoMoN and CoMoC catalysts exhibit higher total hydrogen consumption values, namely 1.35 and 1.31 mmol H_2/g STP, respectively, compared to the CoMo catalyst with a value of 0.99 mmol H_2/g STP. This trend is consistent with the degree of reduction and the formation of a thermally stable $CoAl_2O_4$-structure in the CoMo catalyst. The higher total hydrogen consumption and degree of reduction for the CoMoN and CoMoC catalysts, in comparison to the CoMo catalyst, suggest that the carbiding and nitriding treatments facilitate the formation of the active phase.

3.2. Physicochemical characterization of reduced catalysts

3.2.1. CO chemisorption on reduced catalysts

Metal dispersion and metallic surface area after reduction at 400 °C are critical parameters that can affect catalytic performance. It has been recognized in the literature that CO uptake provides a reliable indication of the concentration of active sites responsible for the CO oxidation reaction [62]. Furthermore, CO uptake data provide information on the chemisorption capacity of the catalysts' surfaces, which can be related to the active diameter of the adsorption sites that are present if the CO adsorption stoichiometry is known. However, CO chemisorption on Co-supported catalysts is a very complex phenomenon, since different binding stoichiometries may co-exist, including those corresponding to adsorbed CO molecules in bridged (tilted) and linear configurations, and even subcarbonyl [63]. In the case of CoMoC catalysts, it is usually considered that CO is molecularly adsorbed on the terminated surface defect sites [64], but the binding geometry is not that clear in the case of CoMoN catalysts, especially when Co_3Mo_3N phases are formed [65], as in the present study (see the HRTEM images in Fig. 3). Due to this, the discussion of the CO chemisorption results will be centered on the CO uptake values of the CoMo, CoMoC, and CoMoN catalysts (see Table 4).

The CoMoC catalyst exhibited the highest CO uptake (20.1 μmol CO/g_{cat}), followed by CoMoN (10.8 μmol CO/g_{cat}) and CoMo (3.6 μmol CO/g_{cat}) catalysts. Furthermore, the CoMoN and CoMoC catalysts also showed the highest metallic surface area and metal dispersion (see Table 4). Therefore, the combination of higher metal dispersion and metallic surface area, together with higher CO adsorption capacity in these catalysts could indicate a better distribution of active sites, which in turn may contribute to their enhanced catalytic activity.

3.2.2. Surface interactions of CO and NO molecules on reduced catalysts

An *in-situ* DRIFTS spectroscopy analysis was used to examine the surface properties of the reduced catalysts and their interaction with the probe molecules. To establish a baseline, an experiment was conducted in which CO and NO were adsorbed on the Al_2O_3 support. However, no infrared bands corresponding to adsorbed CO or NO were observed. Therefore, Fig. 7a and b only present the spectra of CO and NO adsorbed on reduced CoMo, CoMoN, and CoMoC catalysts at 400 °C, a temperature corresponding to the more active conditions [66].

CO-DRIFTS spectra of the reduced CoMo, CoMoN, and CoMoC catalysts show similar CO adsorption bands between 1900 and 2300 cm^{-1}, attributed to the $Mo^{\delta+}$-CO interactions (Fig. 7a). However, the absence of the expected $Co^{\delta+}$-CO signal ($0 < \delta < 1$) at 2060 cm^{-1} could be attributed to the low Co content in the catalysts or the CO's preference for adsorption on Mo sites (higher adsorption energy compared to Co), as will be demonstrated later through DFT calculations. A significant ν_{CO} absorbance at 2170 cm^{-1} can be ascribed to the presence of CO adsorbed onto coordinatively unsaturated (cus) $Mo^{\delta+}$ sites ($2 < \delta < 4$) [67,68]. Two additional bands located at 2110 and 2044 cm^{-1} are attributed to linearly adsorbed CO on surface cus-Mo^{3+} and cus-$Mo^{\delta+}$ ($0 < \delta < 2$) sites, respectively. The weak shoulder observed at 2026 cm^{-1}, associated with linearly adsorbed CO on the surface of $Mo^{\delta+}$ ($0 < \delta < 1$) atoms, is only observed in the CoMo catalyst [66]. As previously reported for Al_2O_3-supported Mo_2N [68] and Mo_2C [69] catalysts, these findings indicate that a significant portion of surface Mo-sites are still in a high valence state, suggesting that the catalysts maintain their surface as oxy-nitrides and oxy-carbides [68,69]. On the other hand, the spectra of CoMoN and CoMoC catalysts showed some unidentified signals. The CoMoC catalyst presents a weak signal at 1788 cm^{-1}, while the CoMoN catalyst shows two intense bands in 1868 and 1788 cm^{-1}. The similar band at 1788 cm^{-1} is more intense in the CoMoN catalyst compared to the CoMoC catalyst. This provides evidence that these catalysts have additional adsorption surface sites which are necessary and should be explored rationally soon.

NO-DRIFTS experiments are more frequently employed as a test due to the NO molecule suitability for assessing the presence of vacancies on transition-metal catalysts [70]. The spectra of the reduced CoMo, CoMoN, and CoMoC catalysts also have similar NO adsorption bands, appearing between 1500 and 1900 cm^{-1}, due to the $Co^{\delta+}$-NO and $Mo^{\delta+}$-NO interactions (Fig. 7b). The signal at a high wavenumber (1872 cm^{-1}) is produced by the symmetric vibration of the dinitrosyl

Table 3
Hydrogen consumption and degree of the reduction (α) determined from H_2-TPR profiles.

Catalysts	H_2 consumption (mmol H_2/g STP)			α
	200–600 °C	600–950 °C	Total	
CoMo	0.35	0.64	0.99	0.38
CoMoN	0.47	0.88	1.35	0.52
CoMoC	0.33	0.98	1.31	0.51

Table 4
CO chemisorption parameters of the catalysts reduced at 400 °C.

Catalysts	CO uptake (μmol CO/g_{cat})	Metal dispersion (%)	Metallic surface area (m^2/g_{metal})
CoMo	3.6	0.5	2.2
CoMoN	10.8	2.5	12.3
CoMoC	20.1	1.4	6.8

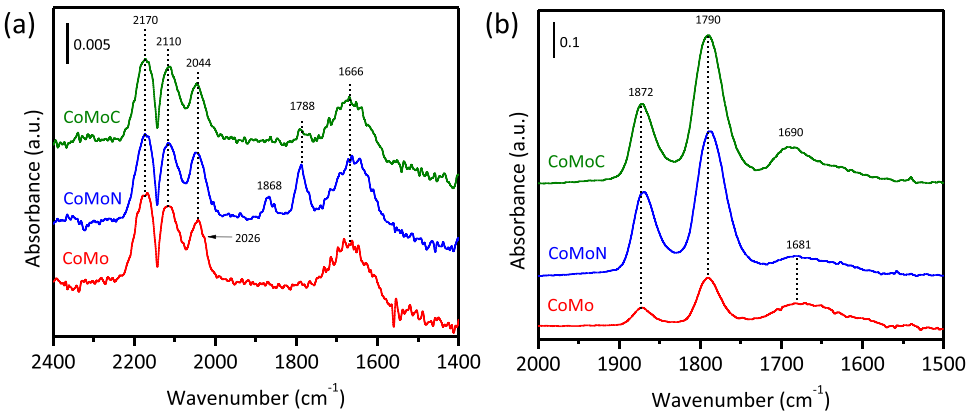

Fig. 7. *In situ* characterization of the probe molecules-catalyst interaction via DRIFTS spectra on catalysts reduced at 400 °C. (a) CO-catalyst and (b) NO-catalyst interactions.

group on Co-sites, while the band at an intermediate wavenumber (1790 cm^{-1}) is the overlap of the asymmetric vibration of dinitrosyl on Co sites and the symmetric vibration of dinitrosyl on Mo-sites. Furthermore, a signal appears at the lower wavenumber (1690 cm^{-1}), which is assigned to the asymmetry vibration of dinitrosyl species interacting with Mo-sites [66]. Although the positions of the signals appear to be similar, there is a notable difference in the relative intensity observed among the spectra. The CoMoN and CoMoC catalysts adsorb more reactive species on their surface compared to the CoMo analog, indicating the presence of more active sites with electron-deficient characteristics. This is particularly evident at the Co-sites, which agrees with the observed decrease in the signal intensity in UV–vis DRS spectra associated with inactive $CoAl_2O_4$ spinel.

3.3. Catalytic tests

The catalytic performances of CoMo, CoMoN, and CoMoC catalysts were tested in the CO oxidation reaction using temperature-programmed reaction. The impact of reaction conditions, such as the reduction temperature (Tr, Fig. 8a), the catalyst or catalytic phase (Fig. 8b), the gas hourly space velocity (GHSV, Fig. 8c), and the reduction time (tr, Fig. 8d), were studied. Comparison of the catalysts' performance was assessed by different means. The temperature at which 50% conversion is achieved (T_{50}), is a critical measure of catalytic performance. Lower T_{50} values indicate that the reaction reaches half its completion at a lower temperature, which is generally desirable in this reaction type. In the same way, activation energy (E_a) is another crucial factor in understanding catalytic performance. A lower E_a means less energy is needed for the reaction to start, which can also enhance the

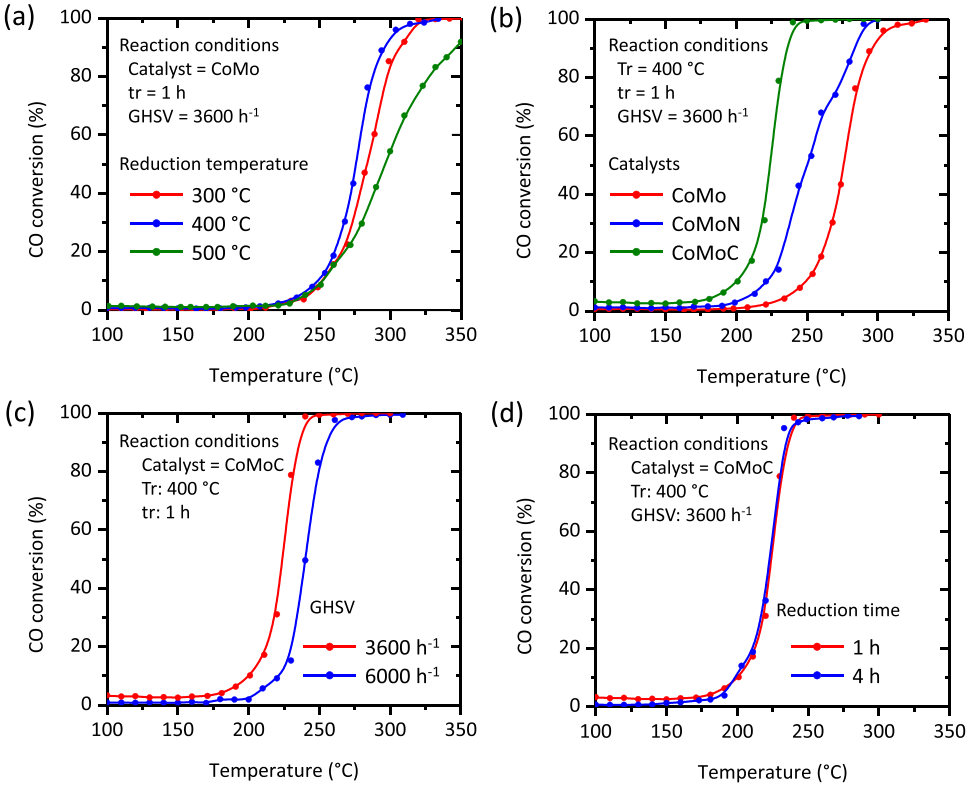

Fig. 8. Effect of experimental conditions on the temperature-programmed CO oxidation performance: (a) reduction temperature, (b) catalyst or catalytic phase, (c) gas hourly space velocity, and (d) reduction time. Shared operating conditions for every set of experiments are detailed in the inset.

efficiency and economy of the reaction.

All CO conversion curves shown in Fig. 8, illustrate the percentage of CO molecules converted into CO_2 as a function of reaction temperature. At the beginning of the reaction, CO conversion was almost negligible. As the reaction temperature increased, CO conversion to CO_2 took place by catalyst action. Furthermore, blank experiments (not shown here) conducted in the reactor at the same experimental conditions but without a catalyst confirmed that non-catalytic CO oxidation was negligible in the whole temperature range considered. The results clearly demonstrate that changes in reaction conditions and the catalyst type led to significant shifts in the catalytic behavior. A summary of the reaction conditions and kinetic parameters obtained is provided in Table 5.

The CoMo catalyst was selected to investigate the impact of the reduction temperature (Tr), while keeping two reaction conditions constant throughout the tests (tr = 1 h and GHSV = 3600 h^{-1}). The T_{50} values decreased from 283.6° to 276.0°C and then increased again to 296.4 °C as Tr increased. The apparent activation energies (E_a) derived from the reaction data showed the same trend. The E_a values were 123.1, 111.7, and 130.7 kJ/mol as Tr increased from 300 to 400 and then 500 °C. These findings suggest that a Tr of 400 °C produces more active catalysts. Furthermore, to explore the influence of the catalyst type, the remaining reaction conditions were held constant, including Tr at 400 °C, tr at 1 h, and GHSV at 3600 h^{-1}. The CoMoC and CoMoN catalysts appear to be more active than the CoMo analog. These catalysts presented E_a values of 76.9 and 104.0 kJ/mol under the mentioned reaction conditions. Although the transformation from CoMo to CoMoN decreased T_{50} from 276.0 to 250.0°C, the value decreased even further in the CoMoC catalyst to 223.6 °C. A steeper slope also indicates a faster and more efficient conversion when the CoMoN and CoMoC catalysts were used, while a gradual slope suggests a slower or less effective conversion process in the CoMo catalyst. Since CoMoC exhibited the highest activity, two additional reaction conditions were investigated using this catalyst. While keeping some reaction conditions constant (Tr = 400 °C and tr = 1 h), increasing the GHSV from 3600 to 6000 h^{-1} resulted in an increase in both the activation energy (from 76.9 to 99.8 kJ/mol) and the T_{50} temperature (from 223.6 to 239.8°C). On the contrary, when tr was increased from 1 to 4 h, it did not appear to have a significant impact, yielding similar activation energy (79.9 ± 2.9 kJ/mol) and T_{50} values (223.7 ± 0.1 °C).

The CoMoC catalyst, activated under reduction conditions of 400 °C for 1 h and operating at a GHSV of 3600 h^{-1}, demonstrates the best performance, exhibiting the lowest T_{50} (223.6 °C) and E_a (76.9 kJ/mol) values. Additionally, it is also worth highlighting the superior performance of the CoMoN catalyst when compared to the CoMo analog. Therefore, it appears that the most effective operational conditions result from a combination of various parameters, with both the reduction temperature, space velocity, and the type of catalytic phase playing crucial roles in enhancing the kinetic parameters.

The stability of the CoMo, CoMoN, and CoMoC catalysts is also a significant concern during these types of reactions. Therefore, five additional tests were carried out at GSHV = 3600 h^{-1} to thoroughly investigate the catalysts, and the results are presented in Fig. 9. This figure first displays three of these tests under isoconversion conditions (X_{CO} = 100 %). To achieve this condition, the tests were conducted at different temperatures: CoMo and CoMoN at 350 °C, and CoMoC at 250 °C (see Fig. 9a, b, and c). Additionally, two further tests were carried out under isothermal conditions at 250 °C. As previously shown in Fig. 8, at this reaction temperature, the CoMo, CoMoN, and CoMoC catalysts exhibited conversions of approximately 10, 50, and 100 %, respectively (see Fig. 9c, d, and e).

As shown in Fig. 9a, b, and c, the CoMo, CoMoN, and CoMoC catalysts exhibited high stability at the same initial conversion (X_{CO} = 100 %). All of them showed that the initial activity could be maintained at 100 % for the first 2 h of reaction. Subsequently, the conversion of the CoMo and CoMoC catalysts gradually decreased from 100 to approximately 93 % over the next 4 h on stream, while the CoMoN catalyst did not appear to deactivate during the testing period. In fact, this last catalyst did not show obvious deactivation at 250 °C throughout 6 h of reaction time (Fig. 9e), demonstrating excellent catalytic stability. However, the CoMo catalyst, tested at 250 °C, seems to create new reaction sites, activating slightly in the first hours of reaction (up to 300 min) and then beginning to deactivate without reaching the initial conversion (see Fig. 9d). These results suggest that the tested catalysts exhibited an excellent degree of stability under the used reaction conditions.

Table 5
Summary of experimental reaction conditions and results of main catalytic parameters.

Catalyst	Reaction conditions			Catalytic parameters	
	Tr (°C)	tr (h)	GHSV (h^{-1})	T_{50} (°C)	E_a (kJ/mol)
CoMo	300	1	3600	283.6	123.1
	400	1	3600	276.0	111.7
	500	1	3600	296.4	130.7
CoMoC	400	1	3600	223.6	76.9
	400	1	6000	239.8	99.8
	400	4	3600	223.8	82.8
CoMoN	400	1	3600	250.0	104.0

3.4. Computational approach

Based on the catalytic results mentioned above, the (220)- and (511)-surfaces of a Co_6Mo_6C crystal structure with space group Fd-3 m, as observed by HRTEM (Fig. 3), were selected for obtaining theoretical adsorption energies through Density Functional Theory (DFT) calculations. This selection was made to further investigate the structure-performance relationship between Co_6Mo_6C surfaces and CO molecules. It is believed that the formation of stable electron-transfer channels, based on the strong interaction between CO and the metal adsorption sites, facilitates this process. To understand the correlation between the binding energy of the CO molecule and the selected material, several rational CO bindings to Co- and Mo-sites on the surface were examined (see ESI, Figs. S3 and S4). The most stable CO-bound configurations are shown in Fig. 10.

As an important observation, calculated adsorption energies for all cases are more stable by adding the vdW dispersion to the PBE

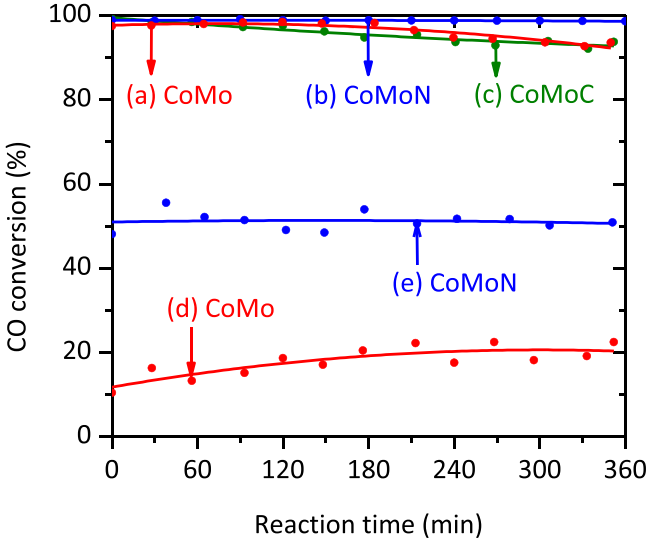

Fig. 9. Stability tests of the catalysts during the CO oxidation reaction at GHSV = 3600 h^{-1} under isoconversion conditions (a, b, and c), and under isothermal conditions (c, d, and e).

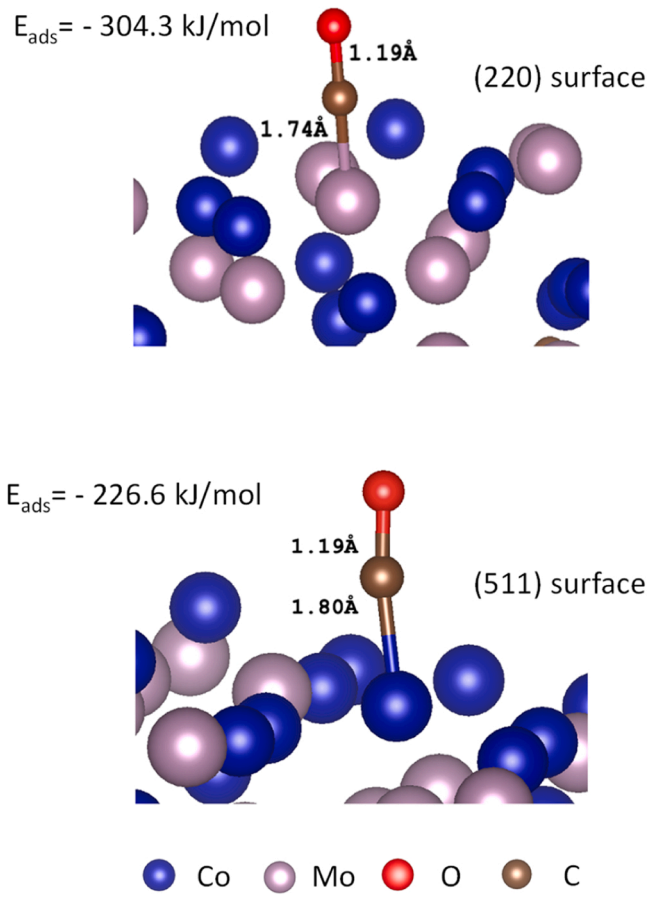

Fig. 10. Lowest energy configurations calculated with DFT of CO chemisorbed on the (220)- and (511)-surfaces of the Co_6Mo_6C crystal structure with space group Fd-3 m (PDF card number 01–080–0338) [37].

functional which should be related to an electrostatic-type interaction. Furthermore, as can be seen in Figs. S3 and S4 in the ESI files, CO chemisorption induces negligible modifications on the surface geometry. This behavior is also observed with both surfaces in the four positions. The binding energies were found to be − 304.3 and − 226.6 kJ/mol for facets (220) in site 4 (p4), and (511) in site 3 (p3), respectively, and agree with previously reported values [71]. The results indicate that the CO adsorption on the Mo-site of the (220) facet is the most efficient because it exhibits the highest adsorption energy (E_{ads} = −304.3 kJ/mol), while on the Co-site (p3) in the (511) surface presents a higher CO adsorption energy (E_{ads} = −226.6 kJ/mol) than other sites, but it is lower than that of Mo in (220) in p4 position. The CO binding energy is inversely proportional to the amount of Mo or Co in the system, since CO can act as both, a donor and an acceptor in chemical reactions, the CO bonding energy should be reduced as the metal d-states are occupied. This correlation highlights the significance of the metal site in influencing CO binding energies, where the Mo-site (p4) on the (220) surface is likely the center of the reaction with the strongest binding affinity for CO. This observation aligns with the DRIFTS experiments where the primary adsorption sites are the Mo sites, and it reinforces established trends that consistently show how the nature of metal sites on a surface, as well as their distribution and quantity, can significantly influence the adsorption behavior of molecules like CO.

3.5. A general discussion about the catalysts' characteristics and their performance

The performance of the CoMoC and CoMoN catalysts was compared to that of representative non-noble metal catalysts. The results demonstrate that our CoMoC catalyst exhibits superior performance, with a lower T_{50} value (T_{50} = 223.6 °C), compared to the reported catalysts, including Cr/Al_2O_3 (T_{50} = 235 °C) [72], Cu/Al_2O_3 (T_{50} = 265 °C) [29], Fe_2O_3/Al_2O_3 (T_{50} = 375 °C) [73], and Ni/Al_2O_3 (T_{50} = 375 °C) [31]. Furthermore, in terms of activation energy, this catalyst also exhibited a lower E_a (76.9 kJ/mol) for CO oxidation than those reported for Fe_2O_3/Al_2O_3 (E_a = 84 kJ/mol) [73] and Co_3O_4 (E_a = 84 J/mol) [74]. This indicates that the carbide catalyst is more effective in promoting CO oxidation reactions at lower temperatures, requiring even less energy to carry out the reaction. The CoMoN catalyst (T_{50} = 250.0 °C) was only outperformed by the Cr/Al_2O_3 catalyst [75]. However, Cr-based catalysts should preferably be avoided due to their high toxicity, posing risks to human health and the environment, and their tendency to undergo deactivation, resulting in reduced catalytic performance over time.

Characterization results could explain the distinct performances, as there are some important characteristics of CoMoN and CoMoC catalysts that could be related to enhanced catalytic performance. The shift in Mo absorption bands towards higher wavelengths observed by the UV–vis DRS technique offers a hint as to why they exhibit enhanced activity, as it may be the initial indication of a greater dispersion by increasing the amount of the octahedral Mo species. The identification of these species was also carried out by the Raman spectra. UV–vis DRS spectra also demonstrated a decrease in the formation of inactive $CoAl_2O_4$-spinel during the CoMoN and CoMoC preparation, suggesting that reducing that spinel formation could be a potential way to increase the amount of Co atoms in their active form, and hence enhance the catalytic activity. The most active catalysts presented the lowest associated-$CoAl_2O_4$ triplet signal, indicating a higher interaction between Co and Mo caused by the formation of a bimetallic Co_6Mo_6C and Co_3Mo_3N structure. The absence of evidence for spinel $CoAl_2O_4$ phase or segregated monometallic phases in HRTEM analyses cannot definitively exclude their presence as limited areas were analyzed by the technique.

The CoMoC and CoMoN catalysts also exhibited higher total hydrogen consumption and a greater degree of reduction compared to the CoMo catalyst, suggesting a more efficient formation of active sites. These H_2-TPR results agree with the CO chemisorption parameters on the reduced catalytic samples, revealing that the carbide and nitride catalysts had the highest CO uptake and metal dispersion and the largest exposed metallic surface area compared to the oxide analogs, suggesting an improved distribution of these active sites. The adsorption sites observed in the CO-DRIFTS spectra appear to be similar, as all catalysts show Mo^{4+}, Mo^{3+}, and $Mo^{\delta+}$ ($0 < \delta < 2$) species interacting with the CO molecules. However, these results could be a piece of evidence that the formation of oxy-nitrides and oxy-carbides species in the nitrides and carbides may contribute to the observed catalytic activity. Furthermore, it is worth noting that the appearance of unidentified signals in CO-DRIFTS spectra in these catalysts may indicate the creation of additional sites; the increase in the signals observed in the NO-DRIFTS spectra could also support this. Furthermore, preliminary theoretical calculations on the Co_6Mo_6C crystal structure with space group Fd-3 m indicated that the CO molecules could interact more effectively with Mo-site (p4) in the (220) surface, while could interact effectively with the Co-site (p3) in the (511) surface.

Our catalysts represent a significant advancement in the field, despite noble metals (Au, Pt, Pd) continuing to outperform them [76–78]. This is because our catalysts offer an advantage in utilizing non-noble metals, which has achieved remarkable progress in making the catalytic process more economically viable. Therefore, it is concluded that the promising results of the CoMoC and CoMoN catalysts pave the way for the further development of highly efficient and cost-effective CO oxidation catalysts. Another advantage of these catalysts lies in the simplicity of the two-step preparation process. Firstly, a facile impregnation process is employed to deposit Co and Mo precursors onto the Al_2O_3 support, allowing for a controlled distribution on the catalyst surface. Then, a temperature-programmed reaction process

is carried out under a controlled atmosphere, such as NH_3 and CH_4/H_2 for CoMoN and CoMoC catalysts, respectively. This step optimizes the pre-reduction and enhances the formation of efficient solids. Consequently, the two-step preparation process provides us with greater control over the catalyst's structure, composition, and surface properties.

4. Conclusions

This study reports for the first-time promising results on the low-temperature catalytic CO oxidation reaction using CoMo nitrides and carbides as catalysts, through the phase transformation from Al_2O_3-supported CoMo catalysts to their nitrides and carbides, under the appropriate reaction conditions. It also reveals the correlation between the kinetic parameters and the catalysts' structures, compositions, morphologies, and surface properties, providing valuable insights into the rational design of catalysts.

The experimental results show that the catalytic performance was influenced by both the catalysts' nature and the reaction conditions, such as the reduction temperature (Tr = 300, 400, and 500 °C) and gas hourly space velocity (GHSV = 3600 and 6000 h^{-1}). The reduction time (tr = 1 and 4 h) did not have a significant impact on the catalysts' behavior during reaction. The CoMoC catalyst outperformed the others with its remarkable performance, marked by the lowest T_{50} and E_a values, while the CoMoN catalyst only exhibited a high performance when compared to the unmodified CoMo catalyst. The optimal performance was achieved at a Tr of 400 °C, tr of 1 h, and a GHSV of 3600 h^{-1}, suggesting a balanced condition for effective catalytic activity. Higher Tr, tr, and GHSV did not result in improved performance, emphasizing the importance of finding the right conditions.

The improved catalytic activity of carbides and nitrides for CO oxidation was attributed to several factors, including its enhanced metal dispersion, metallic surface area, and its remarkable ability to form active adsorbed intermediate species. The unique electronic structure of CoMoC and CoMoN catalysts favored the CO adsorption and the formation of active intermediates, such as oxy-carbides and oxy-nitrides, respectively. The Mo-atoms in these materials had a high oxidation state, which makes them more electrophilic and more likely to interact with the probes. The presence of N and C in the material also stabilizes the negative charge on the CO molecules, making it more reactive. It is important to note that the formation of bimetallic carbide and nitride phases also contributes to the decrease of the catalytically inactive $CoAl_2O_4$-spinel. These findings not only enhance our understanding of the factors influencing catalytic performance in the CO oxidation reaction, but also hold the potential to advance the development of novel and efficient heterogeneous catalysts for a wide range of applications beyond CO oxidation reactions.

CRediT authorship contribution statement

Yanet Villasana: Conceptualization, Project administration, Funding acquisition, Writing - review & editing. **Jorge A. García-Macedo:** Resources, Project administration, Funding acquisition. **Andrea Navarro-Puyuelo:** Methodology, Investigation. **Mourad Boujnah:** Methodology, Investigation. **Inés Reyero:** Methodology, Investigation. **Hugo A. Lara-García:** Methodology, Investigation, Funding acquisition. **Jesús Muñiz:** Methodology. **Fernando Bimbela:** Investigation, Project administration, Funding acquisition, Writing - review & editing. **Luis M. Gandía:** Resources, Project administration, Funding acquisition. **Joaquin L. Brito:** Validation, Writing - review & editing. **Franklin J. Méndez:** Conceptualization, Methodology, Formal analysis, Visualization, Supervision, Investigation, Visualization, Project administration, Funding acquisition, Data curation, Writing - original draft.

Declaration of Competing Interest

The authors declare that they have no known competing financial interests or personal relationships that could have appeared to influence the work reported in this paper.

Data availability

Data will be made available on request.

Acknowledgements

All authors would like to express our sincere appreciation to the Agencia Española de Cooperación Internacional para el Desarrollo (AECID) through the Ikiam-UE-AECID 2018/SPE/0000400194 agreement for funding the research. F.J. Méndez also thanks SIP-IPN for partially supporting the research through the SIP-IPN-20230056 project, while J.A. Garcia-Macedo and H.A. Lara-Garcia thank DGAPA-UNAM through the PAPIIT-IN112622 and PAPIIT-IA107023 projects, respectively. L.M. Gandía, F. Bimbela and the rest of UPNA co-authors would also like to thank the Spanish Agencia Estatal de Investigación (AEI) and Ministerio de Ciencia e Innovación (MICINN), as well as the European Union's NextGenerationEU Funds and the European Regional Development Fund (ERDF/FEDER), for granting additional financial support (Project Refs. PID2021-127265OB-C21 and TED2021-130846B-I00) and for the funding provided to hire A. Navarro-Puyuelo as postdoctoral researcher (Project Ref. PLEC2022-009221). M. Boujnah and J. Muñiz also would like to acknowledge the Supercomputing Department (UNAM) for the computing resources under Projects Ref. LANCAD-UNAM-DGTIC-425 project. Likewise, M. Boujnah (CVU number 1018873) wants to acknowledge CONAHCYT-México for his postdoctoral fellowship. Finally, the authors also thank A. Morales, S. Tehuacanero, D. Quiterio, L. Rendon, and C. Zorrilla from IF-UNAM for their technical assistance, and the use of the Servicio General de Apoyo a la Investigación-SAI, Universidad de Zaragoza (UNIZAR), in particular Dr. Ana Guitart and the rest of the staff at the Servicio de Análisis Químico of UNIZAR for conducting the ICP-OES analyses.

Appendix A. Supporting information

Supplementary data associated with this article can be found in the online version at doi:10.1016/j.jece.2023.111478.

References

[1] WHO: World Health Organization, Air Quality And Health. ⟨https://www.who.int/teams/environment-climate-change-and-health/air-quality-and-health/health-impacts⟩. (Accessed 7 July 2023). 2023.
[2] US EPA: United Stated Environmental Protection Agency, Criteria Air Pollutants. ⟨https://www.epa.gov/criteria-air-pollutants⟩. (Accessed 7 July 2023). 2023.
[3] D.M. Patel, P. Kodgire, A.H. Dwivedi, Low temperature oxidation of carbon monoxide for heat recuperation: a green approach for energy production and a catalytic review, J. Clean. Prod. 245 (2020), 118838, https://doi.org/10.1016/j.jclepro.2019.118838.
[4] J.R. Rostrup-Nielsen, Syngas in perspective, Catal. Today 71 (2002) 243–247, https://doi.org/10.1016/S0920-5861(01)00454-0.
[5] H.J. Kim, M.G. Jang, D. Shin, J.W. Han, Design of ceria catalysts for low-temperature CO oxidation, ChemCatChem 12 (2020) 11–26, https://doi.org/10.1002/cctc.201901787.
[6] F. Feyzbar-Khalkhali-Nejad, E. Hassani, A. Rashti, T.-S. Oh, Adsorption-based CO removal: principles and materials, J. Environ. Chem. Eng. 9 (2021), 105317, https://doi.org/10.1016/j.jece.2021.105317.
[7] A.H. Hatta, A.A. Jalil, N.S. Hassan, M.Y.S. Hamid, A.F.A. Rahman, L.P. Teh, D. Prasetyoko, A review on recent bimetallic catalyst development for synthetic natural gas production via CO methanation, Int. J. Hydrog. Energy 47 (2022) 30981–31002, https://doi.org/10.1016/j.ijhydene.2021.10.213.
[8] S. Royer, D. Duprez, Catalytic oxidation of carbon monoxide over transition metal oxides, ChemCatChem 3 (2011) 24–65, https://doi.org/10.1002/cctc.201000378.
[9] P. Jing, X. Gong, B. Liu, J. Zhang, Recent advances in synergistic effect promoted catalysts for preferential oxidation of carbon monoxide, Catal. Sci. Technol. 10 (2020) 919–934, https://doi.org/10.1039/C9CY02073J.

[10] Y. Liao, H. Xu, Z. Li, L. Ji, L. Wang, G. Gao, W. Huang, Z. Qu, N. Yan, Boosting RuO_2 surface reactivity by Cu active sites over Ru/Cu-SSZ-13 for simultaneous catalytic oxidation of CO and NH_3, J. Phys. Chem. C 125 (2021) 17031–17041, https://doi.org/10.1021/acs.jpcc.1c04100.
[11] K.C. Taylor, Automobile catalytic converters, Stud. Surf. Sci. Catal. 30 (1987) 97–116, https://doi.org/10.1016/S0167-2991(09)60416-X.
[12] D. Chen, H. Lei, W. Xiong, Y. Li, X. Ji, J.-Y. Yang, B. Peng, M. Fu, P. Chen, D. Ye, Unravelling phosphorus-induced deactivation of Pd-SSZ-13 for passive NOx adsorption and CO oxidation, ACS Catal. 11 (2021) 13891–13901, https://doi.org/10.1021/acscatal.1c03214.
[13] H. Zhao, X. Chen, A. Bhat, Y. Li, J.W. Schwank, Insight into hydrothermal aging effect on deactivation of Pd/SSZ-13 as low-temperature NO adsorption catalyst: effect of dealumination and Pd mobility, Appl. Catal. B 286 (2021), 119874, https://doi.org/10.1016/j.apcatb.2020.119874.
[14] F. Cai, S. Shan, L. Yang, B. Chen, J. Luo, C.-J. Zhong, CO oxidation on supported platinum group metal (PGM) based nanoalloys, Sci. China Chem. 58 (2015) 14–28, https://doi.org/10.1007/s11426-014-5264-y.
[15] Y. Zhou, Z. Wang, C. Liu, Perspective on CO oxidation over Pd-based catalysts, Catal. Sci. Technol. 5 (2015) 69–81, https://doi.org/10.1039/C4CY00983E.
[16] J. Lin, X. Wang, T. Zhang, Recent progress in CO oxidation over Pt-group-metal catalysts at low temperatures, Chin. J. Catal. 37 (2016) 1805–1813, https://doi.org/10.1016/S1872-2067(16)62513-5.
[17] F.J. Méndez, M.G. Blanco, J.B. Rosas-Fernández, J.A. García-Macedo, Relationship between Al-loading and CO oxidation activity of mesostructured silica-supported Pt-based catalysts, Microporous Mesoporous Mater. 305 (2020), 110295, https://doi.org/10.1016/j.micromeso.2020.110295.
[18] X. Zhang, Z. Qu, F. Yu, Y. Wang, Progress in carbon monoxide oxidation over nanosized Ag catalysts, Chin. J. Catal. 34 (2013) 1277–1290, https://doi.org/10.1016/S1872-2067(12)60610-X.
[19] S. Dey, G.C. Dhal, D. Mohan, R. Prasad, Advances in transition metal oxide catalysts for carbon monoxide oxidation: a review, Adv. Compos. Hybrid. Mater. 2 (2019) 626–656, https://doi.org/10.1007/s42114-019-00126-3.
[20] S. Dey, G.C. Dhal, Cerium catalysts applications in carbon monoxide oxidations, Mater. Sci. Energy Technol. 3 (2020) 6–24, https://doi.org/10.1016/j.mset.2019.09.003.
[21] I. Hussain, A.A. Jalil, M.Y.S. Hamid, N.S. Hassan, Recent advances in catalytic systems in the prism of physicochemical properties to remediate toxic CO pollutants: a state-of-the-art review, Chemosphere 277 (2021), 130285, https://doi.org/10.1016/j.chemosphere.2021.130285.
[22] K. Eid, A. Gamal, A.M. Abdullah, Graphitic carbon nitride-based nanostructures as emergent catalysts for carbon monoxide (CO) oxidation, Green Chem. 25 (2023) 1276–1310, https://doi.org/10.1039/D2GC02748H.
[23] R. Prasad, P. Singh, A review on CO oxidation over copper chromite catalyst, Catal. Rev. 54 (2012) 224–279, https://doi.org/10.1080/01614940.2012.648494.
[24] S.A. Rasaki, B. Zhang, K. Anbalgam, T. Thomas, M. Yang, Synthesis and application of nano-structured metal nitrides and carbides: a review, Prog. Solid State Chem. 50 (2018) 1–15, https://doi.org/10.1016/j.progsolidstchem.2018.05.001.
[25] I.Z. Koleva, H.A. Aleksandrov, G.N. Vayssilov, Comparison of the reactivity of platinum cations and clusters supported on ceria or alumina in carbon monoxide oxidation, ACS Catal. 13 (2023) 5358–5374, https://doi.org/10.1021/acscatal.3c01146.
[26] B. Zhang, J. Zhou, Z. Sun, New horizons of MBenes: highly active catalysts for the CO oxidation reaction, Nanoscale 15 (2023) 483–489, https://doi.org/10.1039/D2NR05705K.
[27] T.N. Afonasenko, D.V. Yurpalova, Z.S. Vinokurov, A.A. Saraev, E.E. Aidakov, V. P. Konovalova, V.A. Rogov, O.A. Bulavchenko, The formation of Mn-Ce-Zr oxide catalysts for CO and propane oxidation: the role of element content ratio, Catalysts 13 (2023) 211, https://doi.org/10.3390/catal13010211.
[28] B.-Z. Sun, W.-K. Chen, Y.-J. Xu, Reaction mechanism of CO oxidation on Cu_2O (111): a density functional study, J. Chem. Phys. 133 (2010), 154502, https://doi.org/10.1063/1.3489663.
[29] V. Snapkauskienė, V. Valinčius, P. Valatkevičius, Experimental study of catalytic CO oxidation over CuO/Al_2O_3 deposited on metal sheets, Catal. Today 176 (2011) 77–80, https://doi.org/10.1016/j.cattod.2011.02.023.
[30] L. Nguyen, S. Zhang, S.J. Yoon, F. Tao, Preferential oxidation of CO in H_2 on Pure Co_3O_{4-x} and Pt/Co_3O_{4-x}, ChemCatChem 7 (2015) 2346–2353, https://doi.org/10.1002/cctc.201500320.
[31] S.W. Han, D.H. Kim, M.-G. Jeong, K.J. Park, Y.D. Kim, CO oxidation catalyzed by NiO supported on mesoporous Al_2O_3 at room temperature, Chem. Eng. J. 283 (2016) 992–998, https://doi.org/10.1016/j.cej.2015.08.021.
[32] J.A. Rodriguez, F. Illas, Activation of noble metals on metal-carbide surfaces: novel catalysts for CO oxidation, desulfurization and hydrogenation reactions, Phys. Chem. Chem. Phys. 14 (2012) 427–438, https://doi.org/10.1039/C1CP22738F.
[33] D.C. de Carvalho, J.M. Filho, O.P. Ferreira, A.C. Oliveira, E.M. Assaf, Y. Villasana, Synthesis of novel catalytic materials: titania nanotubes and transition metal carbides, nitrides, and sulfides, in: J.M. Domínguez-Esquivel, M. Ramos (Eds.), Advanced Catalytic Materials: Current Status and Future Progress, Springer International Publishing, Cham, 2019, pp. 13–40, https://doi.org/10.1007/978-3-030-25993-8_2.
[34] Y. Villasana, F. Ruscio-Vanalesti, C. Pfaff, F.J. Méndez, M.A. Luis-Luis, J.L. Brito, Atomic ratio effect on catalytic performance of FeW-based carbides and nitrides on thiophene hydrodesulfurization, Fuel 110 (2013) 259–267, https://doi.org/10.1016/j.fuel.2012.11.055.
[35] Y. Villasana, Y. Escalante, J.E. Rodríguez Nuñez, F.J. Méndez, S. Ramírez, M.Á. Luis-Luis, E. Cañizales, J. Ancheyta, J.L. Brito, Maya crude oil hydrotreating reaction in a batch reactor using alumina-supported NiMo carbide and nitride as catalysts, Catal. Today 220–222 (2014) 318–326, https://doi.org/10.1016/j.cattod.2013.10.025.
[36] Y. Villasana, F.J. Méndez, M. Luis-Luis, J.L. Brito, Pollutant reduction and catalytic upgrading of a Venezuelan extra-heavy crude oil with Al_2O_3-supported NiW catalysts: effect of carburization, nitridation and sulfurization, Fuel 235 (2019) 577–588, https://doi.org/10.1016/j.fuel.2018.08.047.
[37] International Center for Diffraction Data, X'pert HighScore Plus software v.3.0 PANalytical, PDF-2 Database, Almelo, Netherlands.
[38] Gatan Inc., DigitalMicrograph Software v.2.32.888.0, Pleasanton, United States.
[39] K. Momma, F. Izumi, VESTA: a three-dimensional visualization system for electronic and structural analysis, J. Appl. Crystallogr. 41 (2008) 653–658, https://doi.org/10.1107/S0021889808012016.
[40] G. Kresse, J. Furthmüller, Efficient iterative schemes for ab initio total-energy calculations using a plane-wave basis set, Phys. Rev. B 54 (1996) 11169–11186, https://doi.org/10.1103/PhysRevB.54.11169.
[41] G. Kresse, J. Hafner, Ab initio molecular-dynamics simulation of the liquid-metal-amorphous-semiconductor transition in germanium, Phys. Rev. B 49 (1994) 14251–14269, https://doi.org/10.1103/PhysRevB.49.14251.
[42] G. Kresse, J. Furthmüller, Efficiency of ab-initio total energy calculations for metals and semiconductors using a plane-wave basis set, Comput. Mater. Sci. 6 (1996) 15–50, https://doi.org/10.1016/0927-0256(96)00008-0.
[43] J.P. Perdew, K. Burke, M. Ernzerhof, Generalized gradient approximation made simple, Phys. Rev. Lett. 77 (1996) 3865–3868, https://doi.org/10.1103/PhysRevLett.77.3865.
[44] S. Grimme, J. Antony, S. Ehrlich, H. Krieg, A consistent and accurate ab initio parametrization of density functional dispersion correction (DFT-D) for the 94 elements H-Pu, J. Chem. Phys. 132 (2010), https://doi.org/10.1063/1.3382344.
[45] G. Leofanti, M. Padovan, G. Tozzola, B. Venturelli, Surface area and pore texture of catalysts, Catal. Today 41 (1998) 207–219, https://doi.org/10.1016/S0920-5861(98)00050-9.
[46] M. Thommes, K. Kaneko, V. Neimark-Alexander, P. Olivier-James, F. Rodriguez-Reinoso, J. Rouquerol, S.W. Sing-Kenneth, Physisorption of gases, with special reference to the evaluation of surface area and pore size distribution (IUPAC Technical Report), Pure Appl. Chem. 87 (2015) 1051–1069, https://doi.org/10.1515/pac-2014-1117.
[47] I. Levin, D. Brandon, Metastable alumina polymorphs: crystal structures and transition sequences, J. Am. Ceram. Soc. 81 (1998) 1995–2012, https://doi.org/10.1111/j.1151-2916.1998.tb02581.x.
[48] H.D. Ruan, R.L. Frost, J.T. Kloprogge, Comparison of Raman spectra in characterizing gibbsite, bayerite, diaspore and boehmite, J. Raman Spectrosc. 32 (2001) 745–750, https://doi.org/10.1002/jrs.736.
[49] T. Mo, J. Xu, Y. Yang, Y. Li, Effect of carburization protocols on molybdenum carbide synthesis and study on its performance in CO hydrogenation, Catal. Today 261 (2016) 101–115, https://doi.org/10.1016/j.cattod.2015.07.014.
[50] D.A. Solís-Casados, L. Escobar-Alarcón, T. Klimova, J. Escobar-Aguilar, E. Rodríguez-Castellón, J.A. Cecilia, C. Morales-Ramírez, Catalytic performance of $CoMo/Al_2O_3$-MgO-Li(x) formulations in DBT hydrodesulfurization, Catal. Today 271 (2016) 35–44, https://doi.org/10.1016/j.cattod.2015.07.046.
[51] E.J. Markel, J.W. Van Zee, Catalytic hydrodesulfurization by molybdenum nitride, J. Catal. 126 (1990) 643–657, https://doi.org/10.1016/0021-9517(90)90027-H.
[52] G. Yan, X. Feng, S.U. Khan, L. Xiao, W. Xi, H. Tan, Y. Ma, L. Zhang, Y. Li, Polyoxometalate and resin-derived P-doped Mo_2C@N-doped carbon as a highly efficient hydrogen-evolution reaction catalyst at all pH values, Chem. Asian J. 13 (2018) 158–163, https://doi.org/10.1002/asia.201701400.
[53] J.-B. Wu, M.-L. Lin, X. Cong, H.-N. Liu, P.-H. Tan, Raman spectroscopy of graphene-based materials and its applications in related devices, Chem. Soc. Rev. 47 (2018) 1822–1873, https://doi.org/10.1039/C6CS00915H.
[54] V.S. Escribano, J.M.G. Amores, E.F. López, M. Panizza, C. Resini, G. Busca, Solid state characterization of coprecipitated alumina-gallia mixed oxide powders, J. Mater. Sci. 40 (2005) 2013–2021, https://doi.org/10.1007/s10853-005-1225-3.
[55] J. Vakros, C. Papadopoulou, G.A. Voyiatzis, A. Lycourghiotis, C. Kordulis, Modification of the preparation procedure for increasing the hydrodesulfurisation activity of the CoMo/γ-alumina catalysts, Catal. Today 127 (2007) 85–91, https://doi.org/10.1016/j.cattod.2007.02.028.
[56] L. Wu, D. Jiao, J.-a Wang, L. Chen, F. Cao, The role of MgO in the formation of surface active phases of $CoMo/Al_2O_3$-MgO catalysts for hydrodesulfurization of dibenzothiophene, Catal. Commun. 11 (2009) 302–305, https://doi.org/10.1016/j.catcom.2009.10.021.
[57] R.S. Weber, Effect of local structure on the UV–visible absorption edges of molybdenum oxide clusters and supported molybdenum oxides, J. Catal. 151 (1995) 470–474, https://doi.org/10.1006/jcat.1995.1052.
[58] F.J. Méndez, O.E. Franco-López, X. Bokhimi, D.A. Solís-Casados, L. Escobar-Alarcón, T.E. Klimova, Dibenzothiophene hydrodesulfurization with NiMo and CoMo catalysts supported on niobium-modified MCM-41, Appl. Catal. B 219 (2017) 479–491, https://doi.org/10.1016/j.apcatb.2017.07.079.
[59] I.V. Yentekakis, G. Goula, P. Panagiotopoulou, S. Kampouri, M.J. Taylor, G. Kyriakou, R.M. Lambert, Stabilization of catalyst particles against sintering on oxide supports with high oxygen ion lability exemplified by Ir-catalyzed decomposition of N_2O, Appl. Catal. B 192 (2016) 357–364, https://doi.org/10.1016/j.apcatb.2016.04.011.
[60] R. López Cordero, F.J. Gil Llambias, A. López Agudo, Temperature-programmed reduction and zeta potential studies of the structure of MoO_3/Al_2O_3 and MoO_3/SiO_2 catalysts effect of the impregnation pH and molybdenum loading, Appl. Catal. 74 (1991) 125–136, https://doi.org/10.1016/0166-9834(91)90013-X.

[61] M. Lu, N. Fatah, A.Y. Khodakov, Optimization of solvent-free mechanochemical synthesis of Co/Al_2O_3 catalysts using low- and high-energy processes, J. Mater. Sci. 52 (2017) 12031–12043, https://doi.org/10.1007/s10853-017-1299-8.
[62] A.D. Allian, K. Takanabe, K.L. Fujdala, X. Hao, T.J. Truex, J. Cai, C. Buda, M. Neurock, E. Iglesia, Chemisorption of CO and mechanism of CO oxidation on supported platinum nanoclusters, J. Am. Chem. Soc. 133 (2011) 4498–4517, https://doi.org/10.1021/ja110073u.
[63] R.C. Reuel, C.H. Bartholomew, The stoichiometries of H_2 and CO adsorptions on cobalt: effects of support and preparation, J. Catal. 85 (1984) 63–77, https://doi.org/10.1016/0021-9517(84)90110-6.
[64] M. Nagai, K. Matsuda, Low-temperature water-gas shift reaction over cobalt-molybdenum carbide catalyst, J. Catal. 238 (2006) 489–496, https://doi.org/10.1016/j.jcat.2006.01.003.
[65] C.D. Zeinalipour-Yazdi, J.S.J. Hargreaves, C.R.A. Catlow, DFT-D3 study of molecular N_2 and H_2 activation on Co_3Mo_3N surfaces, J. Phys. Chem. C 120 (2016) 21390–21398, https://doi.org/10.1021/acs.jpcc.6b04748.
[66] S. Yang, Y. Li, J. Xu, C. Li, Q. Xin, I. Rodriguez-Ramos, A. Guerrero-Ruiz, FTIR study of CO and NO adsorbed on nitrided $CoMo/Al_2O_3$ catalysts, Phys. Chem. Chem. Phys. 2 (2000) 3313–3317, https://doi.org/10.1039/B002557G.
[67] J.L. Brito, B. Griffe, Probing silica-supported Mo^{2+} by means of FT-IR of adsorbed CO, Catal. Lett. 50 (1998) 169–172, https://doi.org/10.1023/A:1019035622997.
[68] S. Yang, C. Li, J. Xu, Q. Xin, Surface sites of alumina-supported molybdenum nitride characterized by FTIR, TPD-MS, and volumetric chemisorption, J. Phys. Chem. B 102 (1998) 6986–6993, https://doi.org/10.1021/jp980660e.
[69] W. Wu, Z. Wu, C. Liang, X. Chen, P. Ying, C. Li, In situ FT-IR spectroscopic studies of CO adsorption on fresh Mo_2C/Al_2O_3 catalyst, J. Phys. Chem. B 107 (2003) 7088–7094, https://doi.org/10.1021/jp027582m.
[70] N.Y. Topsøe, H. Topsøe, Characterization of the structures and active sites in sulfided $CoMoAl_2O_3$ and $NiMoAl_2O_3$ catalysts by NO chemisorption, J. Catal. 84 (1983) 386–401, https://doi.org/10.1016/0021-9517(83)90010-6.
[71] H. Tominaga, Y. Aoki, M. Nagai, Hydrogenation of CO on molybdenum and cobalt molybdenum carbides, Appl. Catal. A 423–424 (2012) 192–204, https://doi.org/10.1016/j.apcata.2012.02.041.
[72] S. Dey, V.V.P. Kumar, Supported and un-supported zinc and chromium oxide catalysts for lower temperature CO oxidation: a review, Environ. Chall. 3 (2021), 100061, https://doi.org/10.1016/j.envc.2021.100061.
[73] J.S. Walker, G.I. Straguzzi, W.H. Manogue, G.C.A. Schuit, Carbon monoxide and propene oxidation by iron oxides for auto-emission control, J. Catal. 110 (1988) 298–309, https://doi.org/10.1016/0021-9517(88)90321-1.
[74] Y.-F.Y. Yao, The oxidation of hydrocarbons and CO over metal oxides. Part III: Co_3O_4, J. Catal. 33 (1974) 108–122, https://doi.org/10.1016/0021-9517(74)90250-4.
[75] M. Cherian, M.S. Rao, W.-T. Yang, J.-M. Jehng, A.M. Hirt, G. Deo, Oxidative dehydrogenation of propane over Cr_2O_3/Al_2O_3 and Cr_2O_3 catalysts: effects of loading, precursor and surface area, Appl. Catal. A 233 (2002) 21–33, https://doi.org/10.1016/S0926-860X(02)00132-1.
[76] R.J.H. Grisel, B.E. Nieuwenhuys, A comparative study of the oxidation of CO and CH_4 over $Au/MO_x/Al_2O_3$ catalysts, Catal. Today 64 (2001) 69–81, https://doi.org/10.1016/S0920-5861(00)00510-1.
[77] A.S. Ivanova, E.M. Slavinskaya, R.V. Gulyaev, V.I. Zaikovskii, OA Stonkus, I. G. Danilova, L.M. Plyasova, I.A. Polukhina, A.I. Boronin, Metal-support interactions in Pt/Al_2O_3 and Pd/Al_2O_3 catalysts for CO oxidation, Appl. Catal. B 97 (2010) 57–71, https://doi.org/10.1016/j.apcatb.2010.03.024.
[78] Y. Chen, Y. Feng, L. Li, J. Liu, X. Pan, W. Liu, F. Wei, Y. Cui, B. Qiao, X. Sun, X. Li, J. Lin, S. Lin, X. Wang, T. Zhang, Identification of active sites on high-performance Pt/Al_2O_3 catalyst for cryogenic CO oxidation, ACS Catal. 10 (2020) 8815–8824, https://doi.org/10.1021/acscatal.0c02253.